Journal of MATERIALS RESEARCH

Article
DOI:10.1557/s43578-022-00536-y

Room-temperature optically detected magnetic resonance of triplet excitons in a pentacene-doped picene single crystal

Fabrizio Moro[1,a], Massimo Moret[1], Alberto Ghirri[2], Andrés Granados del Águila[3], Yoshihiro Kubozono[4], Luca Beverina[1], Antonio Cassinese[5]

[1] Department of Materials Science, University of Milano-Bicocca, via Cozzi 55, 20125 Milan, Italy
[2] Istituto Nanoscienze - CNR, via Campi 213/a, 41125 Modena, Italy
[3] Division of Physics and Applied Physics, School of Physical and Mathematical Sciences, Nanyang Technological University, Singapore, Singapore
[4] Research Institute for Interdisciplinary Science, Okayama University, Okayama 700-8530, Japan
[5] Department of Physics "Ettore Pancini", University of Naples 'Federico II', Piazzale Tecchio, 80, 80125 Naples, Italy
[a] Address all correspondence to this author. e-mail: fabrizio.moro@unimib.it

Received: 2 December 2021; accepted: 3 March 2022

The inclusion of functional molecules as substitutional dopants in single crystals of organic hosts with complementary optical properties provides a versatile strategy to tune optical and magnetic properties in view of their applications in opto-electronics and spintronics. Here, by combining electron spin resonance and optical spectroscopy, isolated triplet exciton states with distinct emission and absorptive resonance modes from two magnetically inequivalent sites of pentacene within the picene crystal are detected at room temperature. This is possible due to the incorporation of a low-doping, 1% mol/mol of pentacene into the monoclinic polymorph of picene high-quality single crystals. In addition, delayed fluorescence—optically detected magnetic resonance (ODMR) studies demonstrate efficient spin-dependent optical activities that are tuned by crystallographically oriented magnetic fields. These properties are particularly appealing for the exploitation of pentacene in room-temperature spin-driven opto-electronics, quantum sensing and in microwave amplification by stimulated emission of radiation (MASER).

Introduction

The preparation of mixed organic crystals provides multifunctional optical, electronic and magnetic properties embedded within the same material system offering opportunities in organic-based devices for applications in opto-electronics [1] and spintronics [2]. The isolation of guest molecules within a host matrix and control of their concentration enable a fine tuning of the intermolecular couplings which in turn may lead to the observation of interesting physical phenomena such as (i) enhanced singlet fission efficiency [3, 4], (ii) isolation of optically excited triplet states robust against decoherence [5] and (iii) energy transfer with up or down energy conversion. [6, 7]

π-conjugated organic materials based on aromatic building blocks such as acenes [8] and phenacenes [9] are at the forefront of current research because they show remarkable photonic and electronic properties such as superconductivity and device performance similar to amorphous silicon [10–12]. Pentacene is one of the most investigated organic molecules within the acene family because of its large spin polarization, long-living optically excited triplet state via intersystem crossing (ISC) at room temperature [8, 13, 14] and long spin coherence time [15]. The optical properties of pentacene-doped *p*-terphenyl single crystals and films have been widely investigated as benchmark for single molecule spectroscopy [16], charge transfer and Frenkel excitons [14], quantum sensing [17], singlet fission [4] and MASER applications by exploiting the inversion of population of the pentacene triplet state [18]. Doping of pentacene in naphthalene has enabled dynamic nuclear polarization as high as 94% [19–21]. In addition, pentacene shows hole mobility comparable to those of amorphous inorganic materials [22, 23] and efficient singlet exciton fission. [24–26].

© The Author(s), under exclusive licence to The Materials Research Society 2022

Phenacenes are noncentrosymmetric versions of acenes consisting of rings fused in angular-oriented structures [11, 27]. Among the phenacene series, picene is the closest structural isomer to pentacene with similar molecular volume and length. These properties make picene the most natural choice for hosting substitutional pentacene molecules. In addition, unlike pentacene, picene is soluble in many common organic solvents and shows intrinsic stability larger than pentacene under atmospheric conditions due to the armchair edges conformation (symmetry: C_{2v}), deep HOMO level (− 5.5 eV) and large bandgap (~ 3.3 eV) [14]. However, the synthesis of phenacenes is less efficient than acenes, as such the studies of their physical properties have progressed at slower pace [12]. Nevertheless, picene has recently attracted a large interest after the discovery of superconductivity [12, 14, 28] and transport properties for field effect transistors both as thin films [9, 29, 30] and heterostructures. [31].

Although pentacene and picene are structural isomers, they show significantly different electronic [32] and optical [11] properties due to the different arrangements of the rings and energy levels misalignment resulting in an overlap between the pentacene absorption spectrum with the picene photoluminescence [33]. So far, doping of picene with pentacene has been realized only in films studied by light absorption and photoluminescence, which have shown robust singlet fission by controlling the spacing between pentacene molecules in a picene matrix [3] and efficient energy transfer from picene to pentacene in films grown by supersonic beams. [14, 33].

Therefore, picene molecules provide a more advantageous host material for pentacene compared to other organic molecules because they (i) protect and isolate pentacene molecules from the environment and from the triplet–triplet interactions, and (ii) provide a means to extend the excitation of pentacene in the ultraviolet region of the electromagnetic spectrum by picene to pentacene energy transfer [33]. The latter mechanism could be exploited in other suitable combinations of phenacenes and acenes with complementary optical properties, thus, opening up the possibility to populate excitonic triplet states by ISC according to the spin statistics under low laser power which otherwise would damage the material.

To the best of our knowledge, no single crystals of pentacene-doped picene have been reported, and the magnetic anisotropy of the pentacene triplet exciton states in a picene host remains unknown. Furthermore, studies on films of pentacene-doped picene have mainly focused on photoluminescence and absorption measurements. However, by combining optical excitation and detection with electron spin resonance (ESR), it is possible to spectroscopically probe and manipulate the energy level populations of the triplet state.

Herein, we report on the spin-dependent optical properties of a pentacene-doped picene single crystal studied by photo-ESR and optically detected magnetic resonance (ODMR). We investigate the magnetic anisotropy and the hyperfine couplings of the excitonic triplet as well as the angular dependence of the light-induced emissive and absorptive resonance modes of the ODMRs. Finally, time-resolved photoluminescence experiments provide compelling evidence that the ODMR signal originates from delayed fluorescence involving optically excited triplets. Our findings demonstrate efficient spin-dependent optical activities of pentacene triplet excitons in a picene matrix. In particular, we observe room temperature and long-living optically spin-polarized states of pentacene triplet excitons which can be tuned by cryptographically oriented magnetic fields on a wide time scale spanning up to milliseconds. Our results shed light on the potential applications of pentacene-doped picene crystals in spin-driven opto-electronics.

Results and discussion

Figure 1(a) shows the crystal structure of picene with views along the *c* and *b* crystallographic axis. From the X-ray diffraction data, we obtained unit cell parameters $a = 8.352(19)$ Å, $b = 6.347(13)$ Å, $c = 13.553(20)$ Å, $\beta = 90.07(13)°$, in space group $P2_1$ (no. 4), which are in agreement with the monoclinic polymorph of pure picene [34–36]. In analogy with what was previously observed in *p*-terphenyl:pentacene crystals, one can assume that the pentacene molecule is substitutional to one of the two *ca*. 60° apart crystallographic equivalent sites of picene, which can take one of these two orientations [37]. In this configuration, the molecular *x*-axis has a unique orientation for all sites, whereas the *y*- and *z*-axes are tilted by 58.37° with respect to each other. The different arrangement of the rings of pentacene and picene [Fig. 1(b)] results in a wider band gap for picene compared to pentacene and favourable alignment of the singlet energy levels for efficient energy transfer [Fig. 1(c)]. [38].

We study the delayed fluorescence signal by performing energy and time-dependent photoluminescence (PL) spectroscopy experiments. Figure 2(a) shows a typical room-temperature photoluminescence excitation (PLE) spectrum that exhibits a high-energy continuum and narrow features in the visible that are attributed to vibronic progressions of the singlet state S_1. The spectral line-narrowing clearly highlights the high quality of our pentacene-doped picene samples. The PL spectra shown in Fig. 2(a) are also distinguished by sharp peaks. Prompt (red curve) and delayed (blue curve) emission profiles taken at zero delay and delay time of 0.1 ms after pulse excitation, respectively, exhibit identical spectral profiles, suggesting light emission on the millisecond time scale due to delayed fluorescence (dFL) involving triplet states.

In order to get more insight on the processes involved onto the dFL, we performed time-resolved experiments by detecting the emissions in a wide time frame spanning μs and hundreads

© The Author(s), under exclusive licence to The Materials Research Society 2022

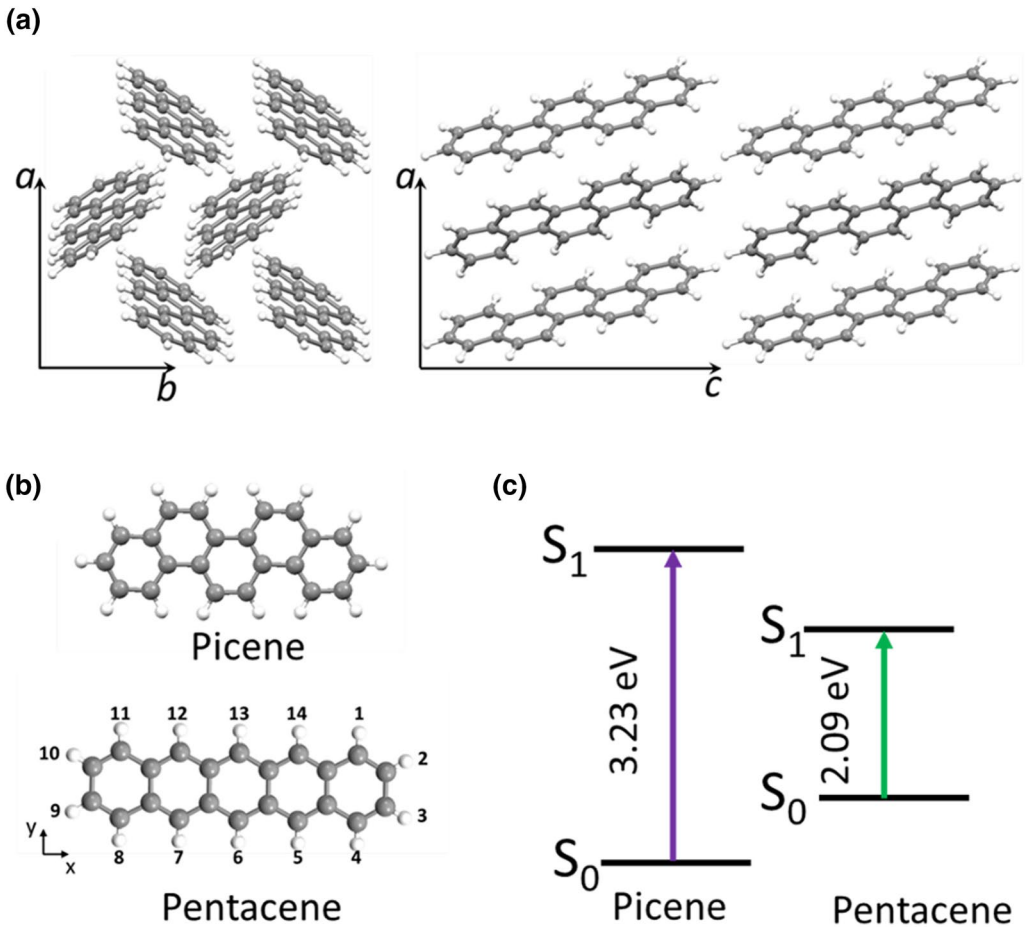

Figure 1: (a) Views along the *c* and *b* crystallographic axis of a picene single crystal. Colour code: white is for hydrogen atoms and grey for carbon atoms. (b) Structures of the picene and pentacene molecules. (c) Relative energy levels of picene and pentacene.

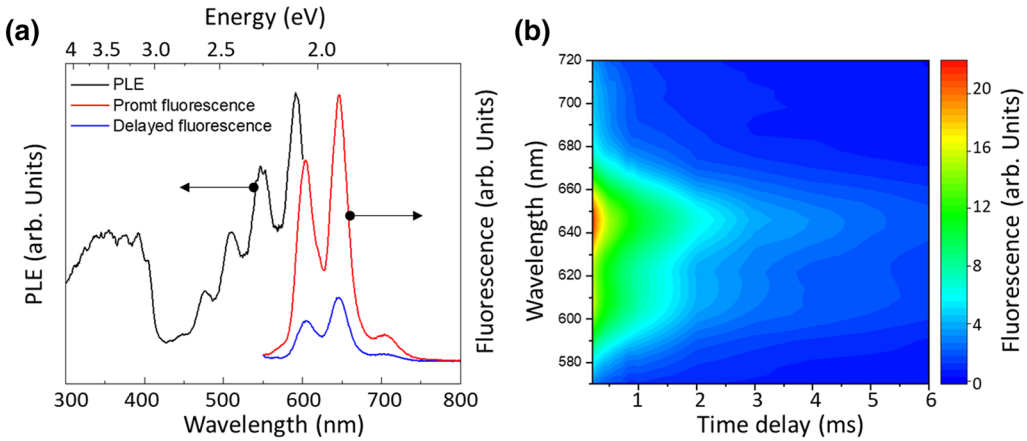

Figure 2: (a) (Left axis) Photoluminescence excitation spectrum (PLE) of pentacene-doped picene recorded at emission wavelength of λ = 645 nm after continuous laser excitation (black curve). (Right axis) Prompt (red curve) and delayed (blue curve) emission spectra taken at 0 and 0.1 ms delay times after 532 nm pulse excitation, respectively. (b) Energy-time fluorescence mapping at millisecond delay times.

of milliseconds. The results reported in Fig. 3 show a complex dynamics with different time constants over six orders of magnitudes (see "Materials and methods" section).

The power dependence recorded at different time delays from the end of the excitation pulse shows a linear dependence for prompt and dFL. (see inset in Fig. 3).

© The Author(s), under exclusive licence to The Materials Research Society 2022

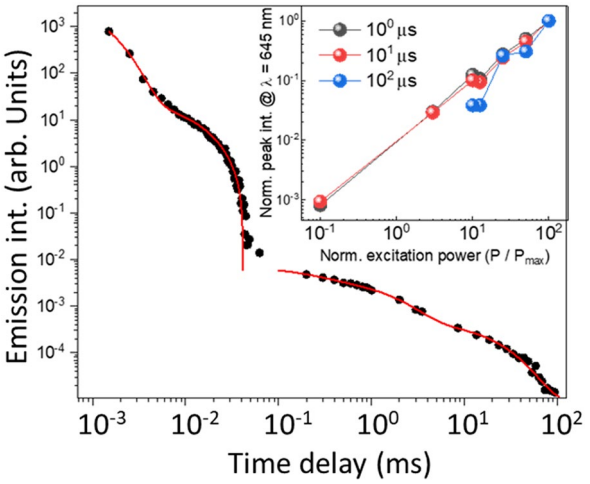

Figure 3: Emission at $\lambda = 645$ nm as function of the delay time between the excitation pulse and the detection along with exponential fittings. Inset: normalized power dependence of dFL at different time delays: 1, 10, and 100 µs.

Figure 4(a) shows the orientation of a pentacene substitutional molecule relative to the picene crystal axes and to the external magnetic field **B** which is rotated by the angle θ around the a-axis, whereas Figs. 4(b) reports the light-induced or photo-electron spin resonance (photo-ESR) spectra of a pentacene-doped picene single crystal recorded at room temperature for an arbitrary angle, $\theta = 64°$. The spectrum shows two pairs of first-derivative resonance lines with an EEAA (where E stands for emission and A for absorption) pattern centred around the g-value = 2, with average full-width-half-maximum (FWHM) linewidth of ~ 3 mT and unresolved hyperfine splitting. The inner and outer lines are separated by ~ 28 mT and ~ 52 mT, respectively. The first-derivative lines are slightly asymmetric due to the rapid passage effect which leads to the dominance of the positive and negative contributions of the first-derivative signal for the low and high field peaks, respectively. The four resonance lines follow a specific path under rotation of the crystal around the a-axis (Fig. 4). The low and high field resonances show a dominant positive (white) and negative (black) contributions, respectively, for $\theta = 90°$ which reverse for $\theta < 40°$.

cw-ESR and photo-ESR narrow magnetic field scans around $g = 2$ and for the lowest field line are reported in Fig. 4(e and f), respectively. The lowest field resonance reveals 5 equally spaced features, whereas the central line has a Lorentzian lineshape with FWHM = 0.4 mT of which resonance field, linewidth and intensity are independent upon laser excitation.

ODMR spectra for the canonical orientations $\theta \sim 0°$ and 90° are shown in Fig. 5(a) whereas in Fig. 5(b) a contour map of the angular-dependent ODMR contrast = ΔPL/PL is reported,

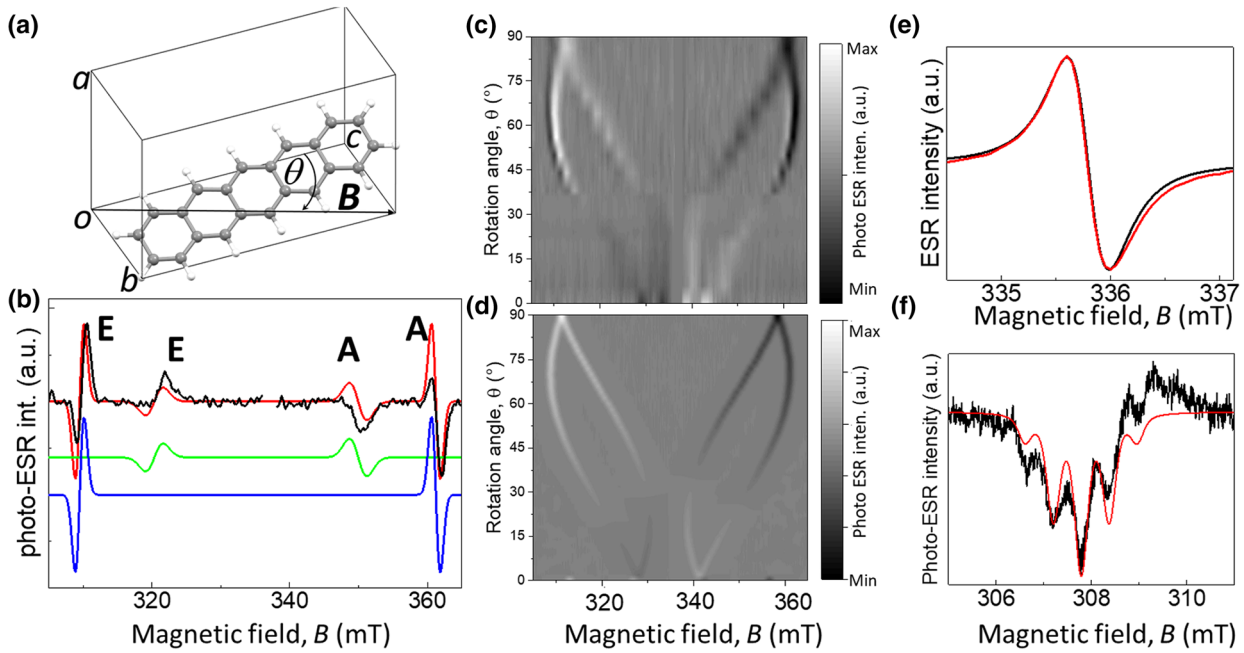

Figure 4: (a) Sketch of the experimental geometry used with the rotation angle θ of the magnetic field relative to the molecular and crystal frames. (b) Photo-ESR spectra recorded at room temperature for $\theta = 64°$ and the corresponding global spectrum simulation (red curve) with the two magnetically inequivalent components in D_{2h} symmetry (green and blue curves). The emissive (E) and absorptive (A) resonance modes are indicated. Road map of the experimental photo-ESR resonance fields (c) and their simulations (d). The colour bar indicates the maximum (white) and minimum (black) intensities in arbitrary units. (e) Narrow magnetic field scan showing the resonance line at $g \sim 2$ in dark condition along with the simulation. (f) Photo-ESR spectrum for $\theta = 80°$ showing the resolved hyperfine splitting due to four equivalent protons. The red curve is the simulation to Eq. 1.

© The Author(s), under exclusive licence to The Materials Research Society 2022

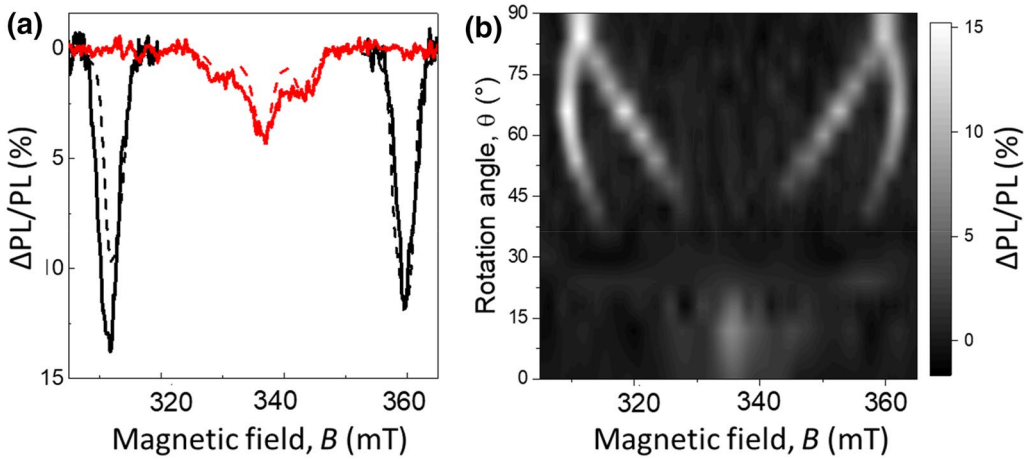

Figure 5: (a) ODMR spectra recorded for $\theta = 90°$ (black line) and 0° (red line) and the corresponding simulations (dashed lines). (b) Map of the ODMR contrast as function of the magnetic field and the rotation angle. The colour bar indicates the ODMR contrast percentage.

where ΔPL is the difference between the photoluminescence signal on and off magnetic resonance condition at a given angle and PL is the off-resonance photoluminescence intensity. The map shows the evolution of ΔPL/PL as function of B and θ. The two resonances observed for $\theta = 90°$ reach the maximum contrast of about 15%, for $\theta < 90°$, they split in four lines and their resonance fields evolve in a similar fashion as reported for the photo-ESR spectra in Fig. 4(c). The ODMR contrast decreases steeply for $\theta < 50°$ until it vanishes and reappears for $\theta \sim 0°$ where the four lines tend to merge close to the free electron g-value.

Photo-ESR and ODMR offer different advantages in the study of triplet exciton states in organic materials and enable to understand different aspects of the same physical process. More specifically, ODMR enables to detect the changes of the photoluminescence under magnetic resonance condition, as such it is sensitive to spin-dependent properties of optical signals. However, due to the selection rules, only optical transitions from energy levels with the same spin quantum number are allowed. In the case of pentacene, when the optical transition $S_0 \rightarrow S_1$ is excited, the system evolves by populating the triplet exciton states from T_N to T_1 manifolds by spin–orbit coupling mediated by ISC, where T_1 is the lowest N state in energy (Fig. 6). The zero-field splitting, D, splits the T_1 state in the substates denoted as T_z, T_x, and T_y of which order depends on the molecular symmetry and sign of D. [39] Due to the selection rules, ODMR is mainly sensitive to the variations of the population of the T_z level [40] as such it does not allow to distinguish between absorptive (A) and emissive (E) modes of the transitions within the Zeeman split triplet states. On the contrary, photo-induced ESR is based on the variation of the cavity Q-value induced by emission of absorption of microwave photons stored into the cavity. Because of the phase-sensitive lock-in detection and magnetic field

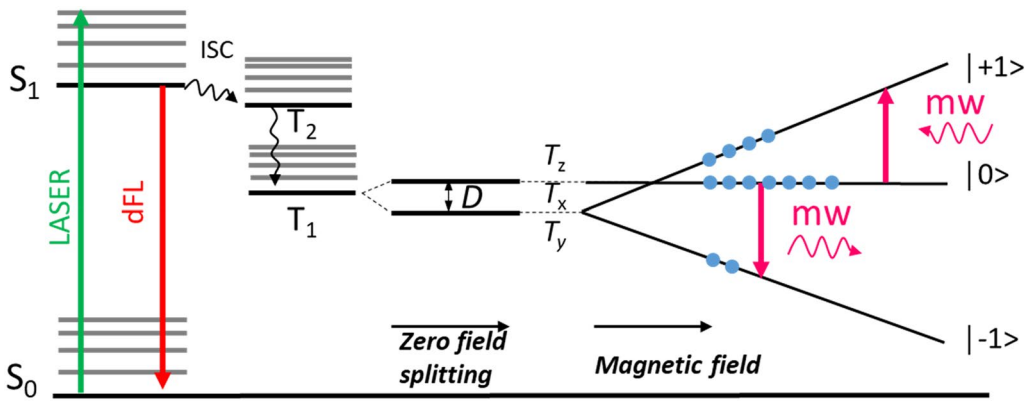

Figure 6: Jablonski energy level scheme, for the magnetic field direction parallel to the molecular z-axis, indicating the intersystem crossing (ISC) with the transfer after internal conversion to the triplet exciton state T_1 sublevels split by zero-field splitting and Zeeman energy in $|0>$, $|+1>$ and $|-1>$. The arrows indicate the photon absorption from the S_0 ground state to the singlet S_1 excited state (green), the Stoke-shifted emission (red) and the microwave (mw)-induced transitions (purple). The circles represent the relative population of energy levels of the triplet exciton.

© The Author(s), under exclusive licence to The Materials Research Society 2022

modulation, a first-derivative spectral line shape is recorded. The sign of the first-derivative lines provides direct evidence for the observation of the emission and absorptive modes. Photo-ESR is sensitive to the out-equilibrium population of the Zeeman split T_1 energy levels.

We simulate the photo-ESR and ODMR spectra of Figs. 4(c) and 5(a) with the spin-Hamiltonian:

$$\widehat{H} = g\mu_B \mathbf{B}\widehat{\mathbf{S}} + DS_z^2 + \sum_i \widehat{\mathbf{S}} A_i \widehat{\boldsymbol{I}}, \quad (1)$$

where g is the spectroscopic g-value, μ_B is the Bohr magneton, $\boldsymbol{B}$ is the magnetic field vector, $\widehat{\mathbf{S}}$ and $\widehat{\boldsymbol{I}}$ are the electron and nuclear spin operators, D is the zero-field splitting and A_i is the hyperfine splitting between the triplet exciton and the i-th nuclei. The best fit was obtained for $S = 1$, $D = 1.46$ GHz, $g = 2$ and assuming non-Boltzmann population of the T_1 states in zero-field $P_{Tx} < P_{Ty} < P_{Tz}$ as well as assuming a $P2_1$ symmetry which provides two magnetically inequivalent sites corresponding to the outer and inner resonance pairs, respectively [Fig. 2(b)]. These findings agree with the two sites tilted by 60° with respect to each other at room temperature of pentacene substitutional to picene within the crystal [37]. The hyperfine coupling contribution will be discussed later.

The fit of the spectral contour plot in Fig. 4(d) allows the determination of the crystal rotation axes and sets the constrains for D tensor frame relative to the molecular frame and the latter relative to the picene crystal and laboratory frames. The D_{2h} symmetry of pentacene makes the D tensor frame to coincide with the molecular frame [41] which, according to our molecular dynamics (MD) simulation (see Experimental Section), is rotated by the Euler angles $\alpha = 26°$, $\beta = 77°$ and $\gamma = -3°$ with respect to the crystal frame [37]. We obtain a good fit of the road map with the Euler angles $\alpha' = 12°$, $\beta' = 60°$ and $\gamma' = 0°$ [Fig. 4(d)], thus, suggesting that pentacene molecules substitute picene within the crystal in one of the two sites and that the different conformation of pentacene with respect to picene makes the former to find a slightly different orientation within the crystal to minimize its potential energy. The molecular x-axis is the same for all the sites within the crystal, whereas the y- and z-axes of the two pentacene sites are not parallel to each other and cause the appearance of four resonance lines for an arbitrary angle upon rotation of the crystal around the a-axis. The coincidence of the inner and outer resonance fields obtained for $\theta \sim 0°$ and 90° indicates that **B** is parallel and perpendicular to the molecular x-axis, respectively [Fig. 4(a)]. We also expect to observe two resonance lines occurring at a magnetic field spectral separation of $2D$; however, their intensities are below the noise level and could not be observed. In addition, the estimated value for $D = 1.46$ GHz matches well the values previously reported for pentacene in other host matrices [42], and it differs significantly from the value $D = 2.7$ GHz reported for picene in p-terphenyl [43]. On the other hand, the EEAA pattern observed in the photo-ESR spectra for pentacene in picene is similar for the pentacene in p-terphenyl but different from the EAEA observed for pentacene in benzoic acid, thus, revealing the influence of the host matrix in determining the inversion of the population. [44].

The emissive (white) and absorptive (black) modes of the photo-ESR resonance lines in Fig. 4(c) are well reproduced by the spectral simulations made by integrating the calculated ESR intensities. In particular, we note that the positive and negative signals decrease in intensities by rotating the crystal away from $\theta = 90°$ until they vanish and switch for $\theta \sim 40°$. We ascribe this behaviour to the mixing of the m_s states which breaks the ESR selection rules leading to a decrease of the transition probabilities and to a redistribution of the population of the energy levels. This is an interesting feature because emissive and absorptive modes can be selected both by magnetic field intensity and orientation with respect to the molecular or crystal frame. The ESR signal observed in dark conditions in Fig. 4(e) could be fitted with a Lorentzian function, and it is independent on the magnetic field orientation. We ascribe this signal to unknown paramagnetic impurities in the picene-pentacene system. The linewidth of the central line upon laser excitation is unchanged despite the formation of exciton triplets. We argue that this could be explained by the weak interaction between localized paramagnetic impurities and the exciton triplets which is below the instrumental sensitivity.

We note that ESR signal in dark was reported in pentacene and picene films in FETs only after the application of a gate voltage, V_g. [45, 46] These observations suggest interesting transport properties which were not observed in other pentacene's host organic materials.

The resolved hyperfine quintet with intensity pattern 1–4–6–4–1 in the photo-ESR spectrum for $\theta \sim 80°$ in Fig. 4(f) is ascribed to hyperfine interactions between the triplet exciton and four equivalent protons of the pentacene molecule. In the general case, both isotropic and anisotropic hyperfine interactions contribute to the experimental spectrum. The isotropic hyperfine coupling is due to the finite probability of the unpaired electron being at the nucleus whereas the anisotropic contribution arises from the electron-nuclear spin dipolar interaction. Both the isotropic and anisotropic interactions can be observed in the solid-state samples, whereas for paramagnetic species in solution, only the isotropic contribution can be observed because the anisotropic contribution average to zero due to the fast tumbling.

From the photo-ESR spectra in Fig. 4(c), we observe that the linewidth of the resonance lines is ~ 5 mT for $\theta \sim 0°$, then it narrows to ~ 1.5 mT for $\theta \sim 56°$, and it broadens again to ~ 3 mT for θ approaching 90°. This behaviour is ascribed to the proportionality of the dipolar hyperfine interaction (Eq. 2) to the term

© The Author(s), under exclusive licence to The Materials Research Society 2022

$3\cos^2\theta-1$ which gives a finite hyperfine interactions along the principal axes and a vanishing interaction for the magic angle, $\theta \sim 54.7°$.

$$A_{\mathrm{dip}} = \sum_i \frac{\mu_0}{4\pi} \frac{\mu_B \mu_N g_e g_N}{h r_i^3} [3(\cos\theta)^2 - 1]. \quad (2)$$

The larger linewidth for $\theta \sim 0°$ compared to that at 90° suggests that the principal hyperfine tensor along the molecular x-axis (A_{xx}) is larger than the one along the y-axis (A_{yy}) in agreement with previous findings [41]. In proximity to the magic angle, the ESR linewidth is determined by homogeneous and in homogeneous broadening including the contribution from the isotropic hyperfine coupling. Based on these considerations, we simulate the low field resonance line for the ESR spectrum at $\theta \sim 80°$ reported in Fig. 4(f) to Eq. 1 assuming a triplet exciton at the centre of the pentacene molecule interacting with 4 equivalent protons located at the carbon positions 5–7–12–14 with an isotropic and a dipole–dipole hyperfine interactions of ~ 10 MHz and ~ 5 MHz, respectively. The estimated isotropic hyperfine contribution represents only an upper limit. Furthermore, the contribution of the protons at positions 6 and 13 is assumed to be considerably smaller; therefore, we could not unambiguously identified it from the spectrum in Fig. 4(f). The resolved hyperfine interaction reveals its dominant contribution to the overall peak-to-peak linewidth of the ESR spectra, thus, suggesting that other contributions for instance due to triplet–triplet and paramagnetic donors—triplets interactions are below the instrumental sensitivity.

As suggested by the comparison between prompt and delayed photoluminescence spectra, the occurrence of ISC leads to a fluorescence decrease for a time interval related to the resident time of electrons in the T_1 state. When the magnetic resonance condition is satisfied, the population of the T_1 sublevels labelled as T_x, T_y and T_z is changed, thus, leading to a variation of the $T_1 \rightarrow S_0$ decay rates, and hence, to an ODMR signal [47]. In the particular case of pentacene, T_x and T_y levels have shorter decay rates than T_z and microwave transitions $T_x \rightarrow T_z$ and $T_y \rightarrow T_z$ are induced leading to a longer life time of the T_1 state that causes a variation of the light emission intensity. [15, 40] In the presence of a magnetic field and crystal orientation, the T_x, T_y, T_z levels are mixed into a superposition of states and they are labelled as $|0>$, $|+1>$ and $|-1>$. [17, 19, 48] The $|0>$ state indicates the crystal orientation parallel to the applied magnetic field vector.

We observe a maximum ODMR contrast of about 15% for $\theta \sim 90°$, which slowly decreases for $90° < \theta < 50°$ and quickly vanishes for $\theta < 50°$, albeit reappearing for $\theta \sim 0°$. This trend is consistent with the angular-dependent photo-ESR study shown in Fig. 4(c) and confirms the mixing of the T_1 sublevels that changes the ESR transition probabilities. The values for the ODMR contrast are comparable to those reported for pentacene in p-terphenyl although at $T = 1.8$ K [49], and they are relatively high if compared to other organic molecules [50–54] and to those of inorganic systems such as silicon carbide [55] and NV centres in diamond where ODMR contrasts of 2% and 20% have been reported, respectively. [56] Therefore, our results support large inversion of population within the triplet state, a property relevant for nuclear spin polarization and quantum sensing applications [17]. Furthermore, we envisage that by exploiting the energy transfer from picene to pentacene [33], the pentacene triplet exciton state could be excited by low excitation densities and high-energy lasers which will expand the range of potential applications on these compounds, particularly for the development of MASER technologies. [18].

Conclusion

We have reported on a new single crystal made by picene doped with pentacene and characterized its spin and angular-dependent optical properties by ODMR and photo-ESR. We have detected the emissive and absorptive modes of the pentacene triplet exciton states and determined the zero-field splitting, the hyperfine interactions of the triplet exciton with four equivalent protons of the pentacene molecule as well as a dark ESR signal. Finally, we have observed a large ODMR contrast which can be tuned by crystal rotation.

Our findings demonstrate that isolated pentacene molecules in the picene matrix show efficient and tunable spin-dependent optical activities on a broad time-scale range spanning up to milliseconds. Further investigations will be devoted to the study of the population dynamics of the triplet states.

In perspective, we envisage that the optical transfer from picene to pentacene holds the potential to extend the excitation of the triplet exciton of pentacene in the ultraviolet region of the electromagnetic spectrum [57]. These properties are particularly appealing for the exploitation of pentacene in spin-driven opto-electronics applications [58] and sensing [17] as well as in low-power microwave amplification by stimulated emission of radiation (MASER). This is a research topic that we are currently pursuing.

Materials and methods

X-ray diffraction

Red-pink single crystals of pentacene-doped picene suitable for a full physical characterization were obtained via the vertical Bridgman-Stockbarger method. A vial of borosilicate glass (internal diameter, 10 mm; height, 70 mm) was filled with a mixture of pentacene and picene in a stoichiometric ratio of approximately 1:100 mol/mol. Owing to oxygen contamination during growth, the actual concentration of pentacene surviving in the crystal may have been somewhat lower than this. The

© The Author(s), under exclusive licence to The Materials Research Society 2022

vial was flame sealed under reduced pressure (0.01 atm) and lowered through a vertical tube furnace set at 380 °C at a rate of 3 mm h^{-1}. A clean, pink crystal sample of ca. 40 mm length formed, gradually fracturing on cooling to room temperature at a rate of approximately 10 °C h^{-1}. The vial was cracked open, and the crystal sample removed almost intact from it. A single crystalline shard of approximately 5 mm length and prismoid shape was carefully removed from the bulk sample by gently pulling across a clear crystalline fracture. Such a sample was checked with a Rigaku R-Axis II X-ray diffractometer at room temperature with Mo-Kα radiation.

Molecular dynamics

Molecular dynamics (MD) simulations were performed to model the orientation of isolated pentacene molecules doping picene crystals. Unit cell parameters and crystal structure of monoclinic picene were taken from reference [34]. The molecular structure of pentacene was extracted from reference [59]. One molecule of pentacene was introduced as a substitutional defect within the 240 molecules of the MD simulation box. A supercell consisting of $5 \times 6 \times 4$ unit cells along the *a*-, *b*- and *c*-axes was employed to describe the picene crystal with three-dimensional periodic boundary conditions. Simulations were performed using the TINKER8.8.3 package [60] under constant temperature and pressure conditions (NPT), with a duration of 0.5 ns. The force field was OPLS-AA [61, 62] with parameters for bonding and non-bonding interactions for aromatic carbon and hydrogen atoms. Non-bonded interactions were cutoff at 1.8 nm. The Verlet algorithm with a time step of 1 fs was used to integrate the equations of motion. The pressure was maintained constant (1 atm) with a Berendsen barostat, with a coupling constant of 1.0 ps. The temperature was controlled with a Berendsen thermostat and a time constant of 0.1 ps. Relevant observables extracted after equilibration included mass centroids, tilt angle defined by means of the pentacene *x* molecular axis in Fig. 1(b) with respect to the *ab* plane of picene, and Euler angles according to the molecular reference frame of Fig. 1(b) with respect to the unit cell axes of picene *a*, *b* and c^* taken as the fixed frame reference *x*, *y* and *z*, respectively.

ODMR and photo-electron spin resonance

ODMR spectra were recorded at room temperature in a Bruker ELEXYS X-band (9.8 GHz) spectrometer. A shard of a single crystal of picene:pentacene was glued on a flat-shaped end of a quartz tube and inserted into a super-high-Q rectangular resonator placed in between the poles of an electromagnet and provided with a front grid to allow optical access and of a goniometer for fine sample rotation (~ 1°) with respect to the external magnetic field, *B*. The crystal was rotated around the *a* crystal axis from *B* parallel to *c* to *B* parallel to *b*. The rotation of the crystal around the *c*-axis, is particularly challenging due to the reduced crystal size to fit the ESR sample support and the low signal-to-noise ratio. A Coherent—Verdi laser was used to excite the pentacene $S_0 \rightarrow S_1$ transition within the picene single crystal with wavelength $\lambda = 532$ nm and power $P = 500$ mW. The photoluminescence signal was filtered with a 550 nm long-pass filter transparent to Stokes-shifted fluorescence emission, detected by a silicon detector, amplified by a low-noise Stanford SR560 preamplifier and lock-in demodulated by a square-wave modulated microwave excitation with amplitude of ~ 2 W and frequency of 1 kHz. For photo-ESR measurements the spectra were recorded by demodulating the reflected signal from the resonant cavity upon microwave sample absorption by a small oscillating magnetic field with amplitude of 0.1 mT and frequency of 100 kHz. All spectra and resonance field road maps were recorded at room temperature and simulated with the *Easyspin* software. [63].

Fluorescence and time-resolved fluorescence

Optical spectra at room temperature were recorded on an ensemble of pentacene-doped picene single crystals in an Agilent Technologies Cary Eclipse Fluorescence Spectrophotometer equipped with a Xenon lamp with output power of 15 W and a photomultiplier tube (PMT) for detection. Photoluminescence excitation was recorded by detecting the emission at $\lambda_{em} = 645$ nm and by scanning the excitation wavelength in the range $\lambda_{exc} = 300$–600 nm.

Fluorescence and delayed fluorescence were detected with the same $\lambda_{exc} = 532$ nm and spectral emission range $\lambda_{exc} = 580$–800 nm except that for the dFL, the emitted signal was detected after a delay time of 100 μs and integrated for 200 ms with gate time of 5 ms. Lifetime measurements were recorded with the following parameters: $\lambda_{ex} = 532$ nm, $\lambda_{em} = 645$ nm and several delay times to cover a time range of 10^0–10^5 μs. Cutt-off and optical density filters were used in excitation and detection, for both PL and time-resolved experiments. Fittings of the data in Fig. 3: bi-exponential decay in the time range 1–100 μs with time constants $\tau_1 = (8.37 \pm 0.01) \times 10^{-1}$ μs and $\tau_2 = (10.8 \pm 1.9)$ μs with pre-exponential factors $A_1 = (4.57 \pm 0.09) \times 10^3$ and $A_2 = (2.9 \pm 0.4) \times 10^1$, respectively. In the time range 10^2—10^5 μs, a triexponential decay fitting provides the following time constants: $\tau_1 = (1.82 \pm 0.47) \times 10^2$ μs, $\tau_2 = (1.4 \pm 0.1) \times 10^3$ μs and $\tau_3 = (1.95 \pm 0.46) \times 10^4$ μs with pre-exponential factors $A_1 = (3.45 \pm 0.01) \times 10^{-3}$, $A_2 = (3.6 \pm 0.1) \times 10^{-4}$ and $A_3 = (4.9 \pm 0.9) \times 10^{-4}$, respectively.

© The Author(s), under exclusive licence to The Materials Research Society 2022

Acknowledgments

We thank the University of Milano-Bicocca, the Swedish Interdisciplinary Magnetic Resonance Centres (SIMARC) and the Italian MIUR through the Progetto Premiale 2012 "EOS: organic electronics for advanced research instrumentation". We thank Prof. W. M. Chen, Prof. M. Fanciulli and Dr T. Toccoli for reading the manuscript and useful comments.

Data availability

The datasets generated during and/or analysed during the current study are available in the Bicocca Open Archive Research Data repository, https://doi.org/10.17632/ncrnw9d3mg.1

Declarations

Conflict of interest The authors declare no conflict of interest.

References

1. K.J. Baeg, M. Binda, D. Natali, M. Caironi, Y.Y. Noh, organic light detectors: photodiodes and phototransistors. Adv. Mater. **25**(31), 4267 (2013)
2. V.A. Dediu, L.E. Hueso, I. Bergenti, C. Taliani, Spin routes in organic semiconductors. Nat. Mater. **8**(9), 707 (2009)
3. K. Broch, J. Dieterle, F. Branchi, N.J. Hestand, Y. Olivier, H. Tamura, C. Cruz, V.M. Nichols, A. Hinderhofer, D. Beljonne, F.C. Spano, G. Cerullo, C.J. Bardeen, F. Schreiber, Robust singlet fission in pentacene thin films with tuned charge transfer interactions. Nat. Commun. (2018). https://doi.org/10.1038/s41467-018-03300-1
4. D. Lubert-Perquel, E. Salvadori, M. Dyson, P.N. Stavrinou, R. Montis, H. Nagashima, Y. Kobori, S. Heutz, C.W.M. Kay, Identifying triplet pathways in dilute pentacene films. Nat. Commun. (2018). https://doi.org/10.1038/s41467-018-06330-x
5. Y.X. Wang, Z. Liu, Y.H. Fang, S. Zhou, S.D. Jiang, S. Gao, Coherent manipulation and quantum phase interference in a fullerene-based electron triplet molecular qutrit. NPJ Quantum Inf. (2021). https://doi.org/10.1038/s41534-021-00362-w
6. M.C. Hanna, A.J. Nozik, Solar conversion efficiency of photovoltaic and photoelectrolysis cells with carrier multiplication absorbers. J. Appl. Phys. **100**(7), 074510 (2006)
7. H. Kraus, M.C. Heiber, S. Vath, J. Kern, C. Deibel, A. Sperlich, V. Dyakonov, Analysis of triplet exciton loss pathways in PTB7:PC71BM Bulk heterojunction solar cells. Sci. Rep. (2016). https://doi.org/10.1038/srep29158
8. J.E. Anthony, The larger acenes: versatile organic semiconductors. Angew. Chem. Int. Ed. **47**(3), 452 (2008)
9. H. Okamoto, N. Kawasaki, Y. Kaji, Y. Kubozono, A. Fujiwara, M. Yamaji, Air-assisted high-performance field-effect transistor with thin films of picene. J. Am. Chem. Soc. **130**(32), 10470 (2008)
10. G.A. Artioli, F. Hammerath, M.C. Mozzati, P. Carretta, F. Corana, B. Mannucci, S. Margadonna, L. Malavasi, Superconductivity in Sm-doped n phenacenes (n=3,4,5). Chem. Commun. **51**(6), 1092 (2015)
11. H.A. Galue, J. Oomens, W.J. Buma, B. Redlich, Electron-flux infrared response to varying pi-bond topology in charged aromatic monomers. Nat. Commun. **7**, 1–12 (2016)
12. Y. Kubozono, H. Mitamura, X. Lee, X.X. He, Y. Yamanari, Y. Takahashi, Y. Suzuki, Y. Kaji, R. Eguchi, K. Akaike, T. Kambe, H. Okamoto, A. Fujiwara, T. Kato, T. Kosugi, H. Aoki, Metal-intercalated aromatic hydrocarbons: a new class of carbon-based superconductors. Phys. Chem. Chem. Phys. **13**(37), 16476 (2011)
13. M. Bendikov, F. Wudl, D.F. Perepichka, Tetrathiafulvalenes, oligoacenenes, and their buckminsterfullerene derivatives: the brick and mortar of organic electronics. Chem. Rev. **104**(11), 4891 (2004)
14. P. Cudazzo, M. Gatti, A. Rubio, Excitons in molecular crystals from first-principles many-body perturbation theory: picene versus pentacene. Phys. Rev. B. (2012). https://doi.org/10.1103/PhysRevB.86.195307
15. J. Wrachtrup, C. Vonborczyskowski, J. Bernard, M. Orrit, R. Brown, Optically detected spin coherence of single molecues. Phys. Rev. Lett. **71**(21), 3565 (1993)
16. M. Orrit, J. Bernard, Sinlge pentacene molecules detected by fluorescence in a para terphenyl crystal. Phys. Rev. Lett. **65**(21), 2716 (1990)
17. K. Tateishi, M. Negoro, S. Nishida, A. Kagawa, Y. Morita, M. Kitagawa, Room temperature hyperpolarization of nuclear spins in bulk. Proc. Natl. Acad. Sci. USA **111**(21), 7527 (2014)
18. M. Oxborrow, J.D. Breeze, N.M. Alford, Room-temperature solid-state maser. Nature **488**(7411), 353 (2012)
19. D.J. Sloop, H.L. Yu, T.S. Lin, S.I. Weissman, Electron spin echoes of a photoexcited triplet pentacene in paraterphenyl crystals. J. Chem. Phys. **75**(8), 3746 (1981)
20. A. Henstra, T.S. Lin, J. Schmidt, W.T. Wenckebach, High dynamic nuclear polarization at room temperature. Chem. Phys. Lett. **165**(1), 6 (1990)
21. A. Kagawa, M. Negoro, R. Ohba, N. Ichijo, K. Takamine, Y. Nakamura, T. Murata, Y. Morita, M. Kitagawa, Dynamic nuclear polarization using photoexcited triplet electron spins in eutectic mixtures. J. Phys. Chem. A **122**(50), 9670 (2018)
22. O.D. Jurchescu, J. Baas, T.T.M. Palstra, Effect of impurities on the mobility of single crystal pentacene. Appl. Phys. Lett. **84**(16), 3061 (2004)
23. C. Reese, W.J. Chung, M.M. Ling, M. Roberts, Z.N. Bao, High-performance microscale single-crystal transistors by lithography on an elastomer dielectric. Appl. Phys. Lett. **89**(20), 202108 (2006)

© The Author(s), under exclusive licence to The Materials Research Society 2022

24. P.M. Zimmerman, Z.Y. Zhang, C.B. Musgrave, Singlet fission in pentacene through multi-exciton quantum states. Nat. Chem. **2**(8), 648 (2010)
25. A. Rao, M.W.B. Wilson, J.M. Hodgkiss, S. Albert-Seifried, H. Bassler, R.H. Friend, Exciton fission and charge generation via triplet excitons in pentacene/C-60 bilayers. J. Am. Chem. Soc. **132**(36), 12698 (2010)
26. H. Najafov, B. Lee, Q. Zhou, L.C. Feldman, V. Podzorov, Observation of long-range exciton diffusion in highly ordered organic semiconductors. Nat. Mater. **9**(11), 938 (2010)
27. H. Okamoto, S. Hamao, R. Eguchi, H. Goto, Y. Takabayashi, P.Y.H. Yen, L.U. Liang, C.W. Chou, G. Hoffmann, S. Gohda, H. Sugino, Y.F. Liaos, H. Ishii, Y. Kubozono, Synthesis of the extended phenacene molecules, 10 phenacene and 11 phenacene, and their performance in a field-effect transistor. Sci. Rep. **9**, 1–11 (2019)
28. R. Mitsuhashi, Y. Suzuki, Y. Yamanari, H. Mitamura, T. Kambe, N. Ikeda, H. Okamoto, A. Fujiwara, M. Yamaji, N. Kawasaki, Y. Maniwa, Y. Kubozono, Superconductivity in alkali-metal-doped picene. Nature **464**(7285), 76 (2010)
29. S. Gottardi, T. Toccoli, S. Iannotta, P. Bettotti, A. Cassinese, M. Barra, L. Ricciotti, Y. Kubozono, Optimizing picene molecular assembling by supersonic molecular beam deposition. J. Phys. Chem. C **116**(46), 24503 (2012)
30. Y. Shimo, T. Mikami, H.T. Murakami, S. Hamao, H. Goto, H. Okamoto, S. Gohda, K. Sato, A. Cassinese, Y. Hayashi, Y. Kubozono, Transistors fabricated using the single crystals of 8 phenacene. J. Mater. Chem. C **3**(28), 7370 (2015)
31. T. Taguchi, F. Chiarella, M. Barra, F. Chianese, Y. Kubozono, A. Cassinese, Balanced ambipolar charge transport in phenacene/perylene heterojunction-based organic field-effect transistors. ACS Appl. Mater. Interfaces **13**(7), 8631 (2021)
32. T. Hosokai, A. Hinderhofer, F. Bussolotti, K. Yonezawa, C. Lorch, A. Vorobiev, Y. Hasegawa, Y. Yamada, Y. Kubozoro, A. Gerlach, S. Kera, F. Schreiber, N. Ueno, Thickness and substrate dependent thin film growth of picene and impact on the electronic structure. J. Phys. Chem. C **119**(52), 29027 (2015)
33. T. Toccoli, P. Bettotti, A. Cassinese, S. Gottardi, Y. Kubozono, M.A. Loi, M. Manca, R. Verucchi, Photophysics of pentacene-doped picene thin films. J. Phys. Chem. C **122**(29), 16879 (2018)
34. A. De, R. Ghosh, S. Roychowdhury, P. Roychowdhury, Structural-analysis of picene, C22H14. Acta Crystallogr. Sect. C Cryst. Struct. Commun. **41**(JUN), 907 (1985)
35. B. Mahns, O. Kataeva, D. Islamov, S. Hampel, F. Steckel, C. Hess, M. Knupfer, B. Buchner, C. Himcinschi, T. Hahn, R. Renger, J. Kortus, Crystal growth, structure, and transport properties of the charge-transfer salt picene/2,3,5,6-tetrafluoro-7,7,8,8-tetracyanoquinodimethane. Cryst. Growth Des. **14**(3), 1338 (2014)
36. Z.S. Zhao, L.H. Britt, G.K. Murphy, Oxidative, iodoarene-catalyzed intramolecular alkene arylation for the synthesis of polycyclic aromatic hydrocarbons. Chem.-Eur. J. **24**(64), 17002 (2018)
37. J. Lang, D.J. Sloop, T.S. Lin, Orientational anisotropic studies by field rotation technique: near zero-field pulsed EPR experiments of pentacene doped in p-terphenyl. J. Magn. Reson. **176**(2), 249 (2005)
38. J. Dieterle, K. Broch, A. Hinderhofer, H. Frank, J. Novak, A. Gerlach, T. Breuer, R. Banerjee, G. Witte, F. Schreibert, Structural properties of picene-perfluoropentacene and picene-pentacene blends: super lattice formation versus limited intermixing. J. Phys. Chem. C **119**(47), 26339 (2015)
39. N. Hirota, M. Baba, Y. Hirata, S. Nagaoka, ODMR and EPR studies of the triplet-states of aliphatic and aromatic carbonyls. J. Phys. Chem. **83**(26), 3350 (1979)
40. J. Kohler, A.C.J. Brouwer, E.J.J. Groenen, J. Schmidt, Fluorescence detecion of single-molecule magnetic-resonance for penatcene in p-terphenyl - the hyperfine interaction of a single triplet spin with a single C-13 nuclear spin. Chem. Phys. Lett. **228**(1–3), 47 (1994)
41. T. Yago, G. Link, G. Kothe, T.S. Lin, Pulsed electron nuclear double resonance studies of the photoexcited triplet state of pentacene in p-terphenyl crystals at room temperature. J. Chem. Phys. **127**(11), 114503 (2007)
42. T.C. Yang, D.J. Sloop, S.I. Weissman, T.S. Lin, Zero-field magnetic resonance of the photo-excited triplet state of pentacene at room temperature. J. Chem. Phys. **113**(24), 11194 (2000)
43. S.S. Kim, Triplet state of picene in para terphenyl crystals by EPR. Chem. Phys. Lett. **61**(2), 327 (1979)
44. H.L. Yu, T.S. Lin, S.I. Weissman, D.J. Sloop, Time resolved studies of pentacene triplets by electron spin echo spectroscopy. J. Chem. Phys. **80**(1), 102 (1984)
45. T. Oyama, Y.S. Yang, K. Matsuo, T. Yasuda, Effects of chalcogen atom substitution on the optoelectronic and charge-transport properties in picene-type pi-systems. Chem. Commun. **53**(27), 3814 (2017)
46. K. Marumoto, S. Kuroda, T. Takenobu, Y. Iwasa, Spatial extent of wave functions of gate-induced hole carriers in pentacene field-effect devices as investigated by electron spin resonance. Phys. Rev. Lett. (2006). https://doi.org/10.1103/PhysRevLett.97.256603
47. P.G. Baranov, H.J. von Bardeleben, F. Jelezko, J. Wrachtrup, *Magnetic Resonance of Semiconductors and Their Nanostructures: Basic and Advanced Applications* (Springer, Vienna, 2017)
48. T.C. Yang, D.J. Sloop, S.I. Weissman, T.S. Lin, Magnetic effects on the dynamics of organic triplets in the level anti-crossing region. Mol. Phys. **100**(9), 1333 (2002)
49. R. Brown, J. Wrachtrup, M. Orrit, J. Bernard, C. Vonborczyskowski, Kinetics of optically detected magnetic-resonance of single molecules. J. Chem. Phys. **100**(10), 7182 (1994)
50. L.S. Swanson, P.A. Lane, J. Shinar, F. Wudl, Polarons and triplet excitons in poly(paraphenylene)(PPV) and substitued PPV.

© The Author(s), under exclusive licence to The Materials Research Society 2022

An optically detected magnetic resonance study. Phys. Rev. B. **44**(19), 10617 (1991)
51. V. Dyakonov, N. Gauss, G. Rosler, S. Karg, W. Riess, Electron spin resonance in PPV photodiodes detection via photoinduced current. Chem. Phys. **189**(3), 687 (1994)
52. J. De Ceuster, E. Goovaerts, A. Bouwen, V. Dyakonov, Recombination of triplet excitons and polaron pairs in a derived paraphenylene vinylene pentamer. Phys. Rev. B (2003). https://doi.org/10.1103/PhysRevB.68.125202
53. J. Shinar, J. Partee, On the nature of trapped polarons in pi-conjugated polymers. Synth. Met. **84**(1–3), 525 (1997)
54. P.A. Lane, L.S. Swanson, Q.X. Ni, J. Shinar, J.P. Engel, T.J. Barton, L. Jones, Dynamics of photoexticed states in C_{60}. An optically deteced magnetic resonance, ESR and light induced ESR study. Phys. Rev. Lett. **68**(6), 887 (1992)
55. J.F. Wang, J.M. Cui, F.F. Yan, Q. Li, Z.D. Cheng, Z.H. Liu, Z.H. Lin, J.S. Xu, C.F. Li, G.C. Guo, Optimization of power broadening in optically detected magnetic resonance of defect spins in silicon carbide. Phys. Rev. B (2020). https://doi.org/10.1103/PhysRevB.101.064
56. E.V. Levine, M.J. Turner, P. Kehayias, C.A. Hart, N. Langellier, R. Trubko, D.R. Glenn, R.R. Fu, R.L. Walsworth, Principles and techniques of the quantum diamond microscope. Nanophotonics **8**(11), 1945 (2019)
57. S. Fanetti, M. Citroni, R. Bini, L. Malavasi, G.A. Artioli, P. Postorino, HOMO-LUMO transitions in solvated and crystalline picene. J. Chem. Phys. **137**(22), 224506 (2012)
58. T.D. Nguyen, E. Ehrenfreund, Z.V. Vardeny, Spin-polarized light-emitting diode based on an organic bipolar spin valve. Science **337**(6091), 204 (2012)
59. T. Siegrist, C. Kloc, J.H. Schon, B. Batlogg, R.C. Haddon, S. Berg, G.A. Thomas, Enhanced physical properties in a pentacene polymorph. Angew. Chem. Int. Ed. **40**(9), 1732 (2001)
60. J.A. Rackers, Z. Wang, C. Lu, M.L. Laury, L. Lagardere, M.J. Schnieders, J.P. Piquemal, P.Y. Ren, J.W. Ponder, Tinker 8: software tools for molecular design. J. Chem. Theory Comput. **14**(10), 5273 (2018)
61. W.L. Jorgensen, D.S. Maxwell, J. Tirado-Rives, Development and testing of the OPLS all-atom force field on conformational energetics and properties of organic liquids. J. Am. Chem. Soc. **118**(45), 11225 (1996)
62. W.L. Jorgensen, J. Tirado-Rives, Potential energy functions for atomic-level simulations of water and organic and biomolecular systems. Proc Natl. Acad. Sci. USA **102**(19), 6665 (2005)
63. S. Stoll, A. Schweiger, EasySpin, a comprehensive software package for spectral simulation and analysis in EPR. J. Magn. Reson. **178**(1), 42 (2006)

© The Author(s), under exclusive licence to The Materials Research Society 2022